



Asymmetric Lunar Magnetic Perturbations Produced by Reflected Solar Wind Particles

Tian-Xin Zhang^{1,2,3,4} , Hui Zhang^{1,2,3,4} , Hai-Rong Lai⁵ , Jun Zhong^{1,2,3,4} , Li-Bo Liu^{1,2,3,4}, Yong Wei^{1,2,3,4}, Jin-Bin Cao⁶, Jun Cui⁵ , Chang-Bo Zhu⁷, Sui-Yan Fu⁸, and Wei-Xing Wan^{1,2,3,4}

¹ Key Laboratory of Earth and Planetary Physics, Institute of Geology and Geophysics, Chinese Academy of Sciences, Beijing, 100029, People's Republic of China; hzhang@mail.iggcas.ac.cn

² Innovation Academy for Earth Science, Chinese Academy of Sciences, Beijing, 100029, People's Republic of China

³ College of Earth Sciences, University of Chinese Academy of Sciences, Beijing, 100049, People's Republic of China

⁴ Beijing National Observatory of Space Environment, Institute of Geology and Geophysics, Chinese Academy of Sciences, Beijing, 100029, People's Republic of China

⁵ Planetary Environmental and Astrobiological Research Laboratory, School of Atmospheric Science, Sun Yat-sen University, Zhuhai, 519082, People's Republic of China

⁶ School of Space and Environment, Beihang University, Beijing, 100191, People's Republic of China

⁷ Beijing Key Laboratory of Space Environment Exploration, National Space Science Center, Chinese Academy of Sciences, Beijing, 100190, People's Republic of China

⁸ School of Earth and Space Sciences, Peking University, Beijing, 100871, People's Republic of China

Received 2020 February 4; revised 2020 March 31; accepted 2020 April 2; published 2020 April 21

Abstract

Magnetic perturbations characterize the solar wind interaction of the Moon. The solar wind plasma absorption on the dayside surface produces large-scale field perturbations behind, i.e., the field enhancement in the central wake and reduction on the wake boundary. The solar wind repulsion over local lunar magnetic anomalies (LMAs) leads to small-scale magnetic compressions ahead. In this study, the magnetic perturbations around the Moon are examined by using the observations from a near-Moon satellite mission, the Lunar Prospector, and they exhibit a clear left–right asymmetry in a coordinate system related to the solar wind convection electric field (E_{SW}). The magnetic field is observed to enhance before the left terminator that E_{SW} points to, while on the opposite side, it is not. The test particle simulations show that E_{SW} can divert the particles reflected over the LMAs to the left and then the solar wind pickup of these particles leads to the field enhancement observed before the left terminator. Behind the lunar terminator, the wake field reduction is also asymmetric. On the left, the field reduction is more remarkable and located closer to the central wake. The denser plasma, consisting of the background as well as the reflected solar wind particles, may produce a stronger diamagnetic current and thus more significant field reduction there. The asymmetric plasma and magnetic perturbations associated with the reflected particles may be a common and nonnegligible element during the solar wind interaction of a small-scale magnetic field, such as that of an asteroid or a comet.

Unified Astronomy Thesaurus concepts: [Solar wind \(1534\)](#); [Lunar magnetic fields \(960\)](#); [Pickup ions \(1239\)](#)

1. Introduction

The Earth's Moon has been considered as a passive absorber of the incident solar wind particles (Colburn et al. 1967; Ness et al. 1967) because it lacks both an intrinsic global magnetic field and a significant atmosphere. A plasma cavity thus forms behind the Moon known as the lunar wake, and the interplanetary magnetic field (IMF) can pass directly through this celestial body (Ness et al. 1967; Sonett 1982). The magnetic field can be enhanced in the central wake and be reduced in the expansion region surrounding the central wake (Whang & Ness 1970). These magnetic perturbations are produced by diamagnetic currents arising from the pressure gradient across the wake boundary (Ness et al. 1968). The diamagnetic currents, as well as the magnitude of the magnetic perturbations, strongly depend on the solar wind plasma Beta (the ratio of the plasma and the magnetic pressures). The denser solar wind may produce a stronger field enhancement in the central wake and a stronger field reduction in the wake expansion region (Zhang et al. 2012, 2014; Fatemi et al. 2013).

Besides the global perturbations, observations have shown that there are many sporadic lunar magnetic field enhancements on the lunar surface. Despite the lack of a global magnetic field, the Moon possesses regions of local crustal magnetization, i.e., the lunar magnetic anomalies (LMAs; Purucker 2008), with a size varying from tens to hundreds of kilometers (Blewett et al. 2011; Hood et al. 2013) and field magnitude varying from several tens to thousands of nanotesla (nT; Mitchell et al. 2008; Richmond & Hood 2008). Both in situ observations and computer simulations have revealed that the local lunar magnetic enhancements result from the compressional interaction between the LMAs and the incident solar wind (e.g., Sonett & Mihalov 1972; Russell & Lichtenstein 1975; Lin et al. 1998). When standing in the supersonic solar wind, an LMA will act as a small-scale obstacle to the incident solar wind, forming a local magnetic structure above the lunar surface, typically termed as the “mini-magnetosphere” in an analogy to the scenario that the terrestrial magnetosphere interacts with the solar wind (e.g., Hood & Schubert 1980; Harnett & Winglee 2000, 2003; Halekas et al. 2008; Wieser et al. 2010; Lue et al. 2011). When this interaction occurs near the lunar terminator, the resulting field compression is usually termed as the “limb shock,” modified later as the “limb compression,” which can lead to a significant increase in the field magnitude both at the lunar terminator and outside the downstream lunar

wake (Russell & Lichtenstein 1975; Lin et al. 1998; Halekas et al. 2006).

The magnetic perturbations near the Moon may not only be produced by the solar wind compression ahead of the LMAs, but also can result from the pickup of the solar wind particles reflected on these LMAs. It is known that 0.1%–1% of the incident solar wind protons can be reflected by the lunar regolith on the unmagnetized lunar surface (Saito et al. 2008; Wieser et al. 2010). By contrast, on the LMAs, the reflection ratio is much higher. The averaged reflection ratio of a typical LMA is as high as 10%, and even up to 50% above the strongest magnetic anomalies (Saito et al. 2010; Lue et al. 2011, 2014; Giacalone & Hood 2015), i.e., the group of the strong anomalies near the South Pole-Aitken basin (SPAB; Hood 2011). Many previous works focused on how the reflected protons are accelerated by the background solar wind or how they are able to enter the lunar wake from dayside (e.g., Futaana et al. 2003; Saito et al. 2008; Zhong et al. 2013). However, the studies on the influence of these particles to the background solar wind, e.g., how the reflected particles decelerate the background solar wind, or how the background IMF embedded within the solar wind is compressed or bent by the deceleration, are relatively scarce (Halekas et al. 2011; Fatemi et al. 2014; Burinskaya 2015). Recently, the effects of the reflected solar wind particles on the background magnetic field are investigated by using global hybrid simulations (Fatemi et al. 2014). It is found that the formation of a strong field enhancement region was associated with the reflected solar wind particles, extending from ahead of an LMA far downstream to outside the lunar wake (Halekas et al. 2014). Halekas et al. (2017) pointed out that the momentum transfer between the reflected solar wind and the background solar wind contributes to these field enhancements, and that the solar wind deflection in the direction against the solar wind convection electric field (E_{SW}) may lead to stronger field amplification while the solar wind deflection along E_{SW} makes the field amplification weaker.

A coordinate system related to both the solar wind velocity and E_{SW} is introduced in this study to analyze the magnetic field observations from the Lunar Prospector (LP). Data show that strong left–right asymmetries are present in both the field enhancement and the reduction near the lunar terminator, and that both the field perturbations are significant near the terminator where E_{SW} points to. Furthermore, a test particle model is established to investigate the contribution of the solar wind particles reflected over an LMA to these magnetic asymmetries. It is concluded that E_{SW} diverts the reflected solar wind particles to the left, forming an asymmetric plasma distribution around the Moon. The solar wind pickup of these reflected particles and the associated strong diamagnetic currents produce stronger field enhancement and reduction, respectively, on the left terminator as observed. The observation data and the coordinate system are briefly introduced in Section 2. Two lunar magnetic enhancement cases observed by LP are presented in Section 3.1, followed by a statistical study of the 1.5 yr LP data in Section 3.2. The test particle model is present in Section 4. The results are summarized in Section 5.

2. Data and Coordinates

The LP mission is a polar orbit satellite with orbits at altitudes of 80–115 km (high altitudes) in 1998 and 15–45 km (low altitudes) from 1999 January to July (Binder 1998). We

use the magnetic field observations from the MAG instrument on board the LP at a 5 s time resolution (Walker & Russell 2013). The upstream solar wind conditions are determined by using the high-resolution (1 minute) data from the Operating Missions as a Node on the Internet (OMNI), which have been shifted to the nose of the Earth’s bow shock and are further shifted by the traveling time of solar wind from the nose of the bow shock to the Moon.

To avoid any bias arising from the variations of the background solar wind and the associated E_{SW} , the “Lunar Solar Wind-Electric Field” (LSE) coordinate system is adopted. The LSE is a right-handed coordinate system with its origin centered at the Moon, the x -axis pointing against the instantaneous solar wind velocity (V_{SW}), the y -axis determined by $\mathbf{B}_{\text{IMF}} \times \mathbf{X}$, and the z -axis completing the orthogonal set through $\mathbf{X} \times \mathbf{Y}$, where \mathbf{B}_{IMF} is the IMF. In this way, E_{SW} ($E_{\text{SW}} = -V_{\text{SW}} \times \mathbf{B}_{\text{IMF}}$) is always in the $-y$ -direction, and the IMF is always parallel to the xz -plane. The nominal Parker spiral magnetic field at the Moon is essentially in the ecliptic plane, and thus the xz -plane should be on average parallel to the ecliptic plane and the y -direction should basically point to the north/south direction or out of the ecliptic plane. The original observations of V_{SW} and \mathbf{B}_{IMF} are given in the selenocentric solar ecliptic (SSE) coordinate system. A Moon-fixed geographic coordinate system, i.e., the selenographic (SEL) coordinate system, is also adopted in this study to calculate the lunar crustal magnetic fields inferred from the model.

3. Observations

3.1. Case Studies

Two LMA events observed by LP on 1999 June 13 (Event I) and 1998 January 31 (Event II) are presented in Figure 1. The subtended angles between the Sun and the Earth as seen from the Moon ($SA_{\text{S-E}}$) for these two events, are 140° and 170° , respectively. This indicates that the Moon in both events is located in the solar wind. Figures 1(a)–(h) show the LP observations for Event I from 2:15 UT to 3:05 UT on 1999 June 13. In this event, LP moves from the north pole to the south along the longitude of about -75° in SSE at an altitude of ~ 30 km (Figure 1(d)). The crustal magnetic fields at an altitude of 10 km above the lunar surface are modeled by Purucker (2008), shown in the maps of Figures 1(f)–(h). The group LMA at the SPAB is seen to be centered at the solar wind zenith angle (SZA) $\sim 35^\circ$ in the LSE coordinate system in this event. The magnetic fields observed by LP highly fluctuate as shown in Figure 1(a) and after 2:39 UT their magnitude increases slightly from an initial value of ~ 5 nT up to 8 nT. The background IMF from the shifted OMNI data is shown in Figure 1(b), and it is seen that the IMF is very stable except for the change at 2:53 UT. This IMF gives a very stable LSE coordinate system, in which LP continues moving from the right terminator to the left via the top terminator as shown in Figures 1(e) and (h). Figure 1(c) gives R_B , the ratio between the magnitudes of the field observed by LP ($|\mathbf{B}_{\text{LP}}|$) and the IMF ($|\mathbf{B}_{\text{IMF}}|$); $R_B = |\mathbf{B}_{\text{LP}}|/|\mathbf{B}_{\text{IMF}}|$, the red curve). Although the ratio always fluctuates, the smoothed ratio in a 4 minute window (the black curve in Figure 1(c)) shows that during the period from 2:39 UT (marked by the vertical dashed line A) to 3:04 UT (marked by the vertical dashed line B) the magnetic field observed near the Moon is enhanced and the ratio is basically 1.4 and up to 1.6. The orbit of LP corresponding to this period

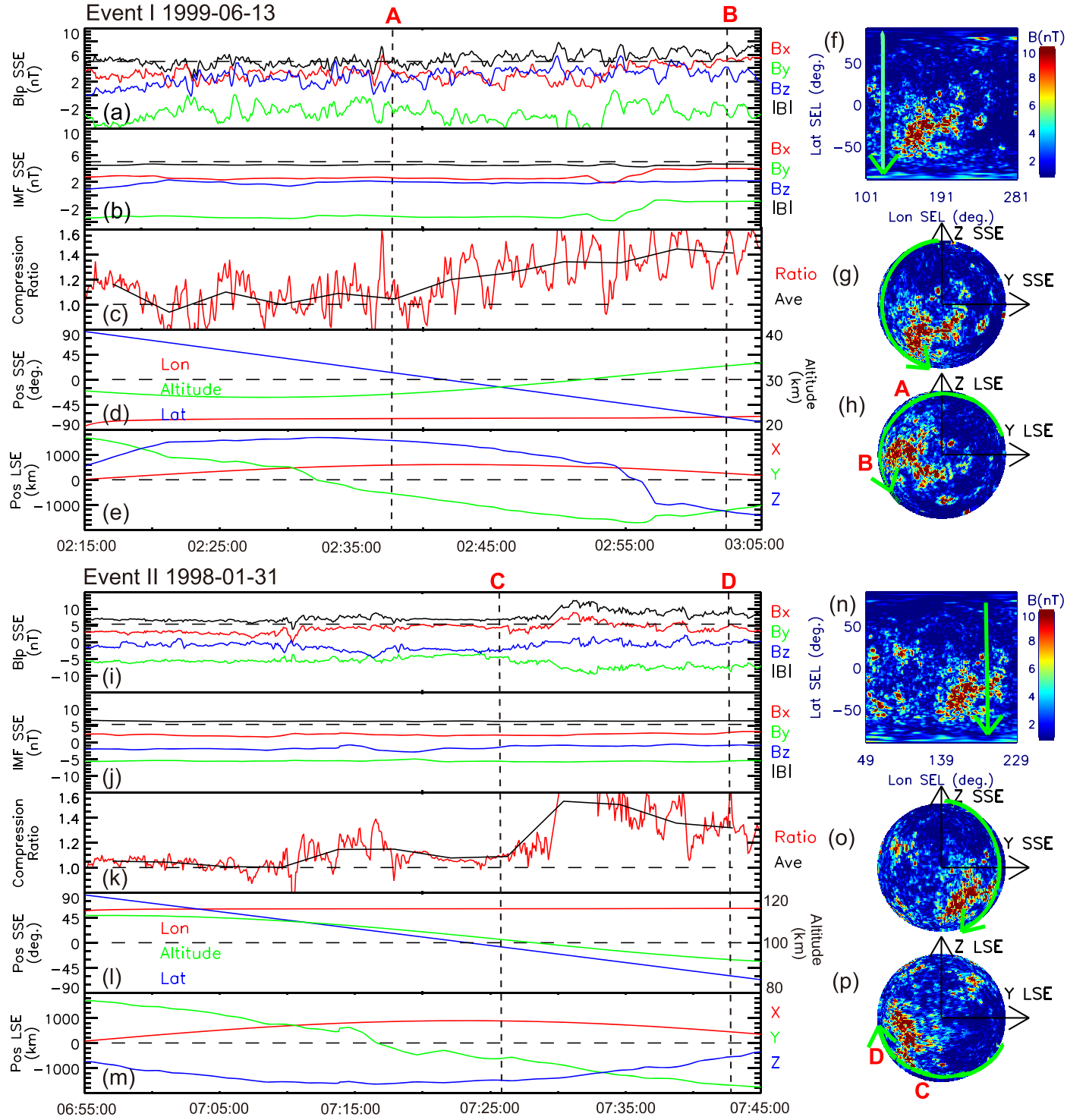


Figure 1. Two representative events of field enhancements, and Event I on 1999 June 13 ((a)–(h)) and Event II on 1998 January 31 ((i)–(p)), respectively. ((a) and (i)) The observed magnetic fields from LP, ((b) and (j)) the corresponding IMF provided by the OMNI and shifted forward or backward by using the time of the solar wind traveling from the nose of the bow shock to the Moon. ((c) and (k)) The compression ratio R_B of the of the magnetic field magnitude at LP to that of the IMF, ((d) and (l)) the position of LP in the SSE coordinate system, ((e) and (m)) the position of LP in the LSE coordinate system, ((f) and (n)) the map of the lunar crustal magnetic fields in the Selenographic coordinate system and the projection of the LP’s trajectory, ((g) and (o)) the projections of the LP’s trajectory and the crustal magnetic fields in the y_z -plane of the SSE coordinate system, and ((h) and (p)) the projections of the LP’s trajectory and the crustal magnetic fields in the y_z -plane of the LSE coordinate system. The vertical dashed lines marked by “A” and “B” in Event I embrace the time period from 2:39 UT to 3:04 UT when LP observed the clear field enhancements. The vertical dashed lines marked by “C” and “D” in Event II denote the field enhancement period from 7:26 UT to 7:43 UT. The corresponding satellite trajectories in these two periods are marked by “A” and “B” in (h) and by “C” and “D” in (p).

of time is embraced by A and B in Figure 1(h), and it is seen that this field enhancement occurs right downstream of the largest SPAB LMA. During this period, the angular separation

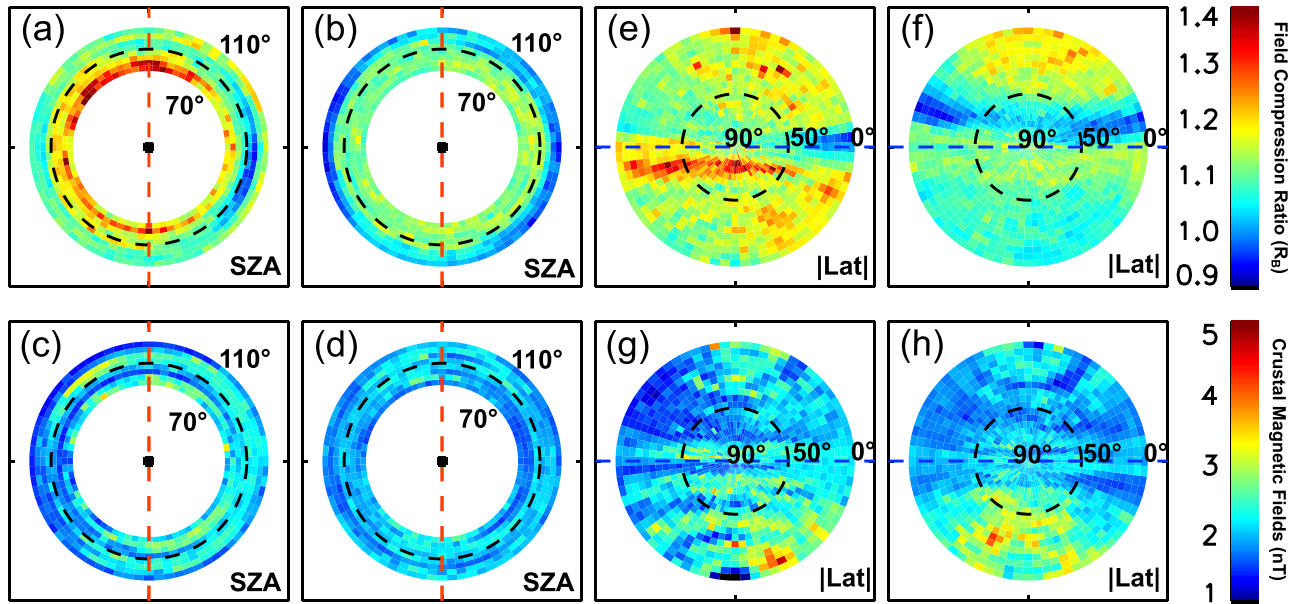


Figure 2. Magnetic field distribution over the lunar surface in the LSE coordinate system with a bin size of $5^\circ \times 5^\circ$. ((a) and (b)) The distributions of the field compression ratio, R_B , within a belt near the lunar terminator with the solar wind zenith angle from 70° to 110° and the heights from 15 to 45 km (a) and from 85 to 115 km (b), respectively, unfolded by the zenith angle to the y_z -plane. ((c) and (d)) The same formats as (a) and (b) but for the distributions of the crustal magnetic fields that are 10 km above the footprint of LP on the lunar surface modeled by Purucker (2008). The black dashed lines denote the lunar terminator, and the red dashed lines divide the plane into left and right in (a)–(d). ((e) and (f)) The xy -plane projections of the field compression ratio, R_B , at low altitudes (15–45 km) and high altitudes (85–115 km), respectively. ((g) and (h)) The xy -plane projections of the distributions of the crustal magnetic fields that are 10 km above the footprint of LP on the lunar surface. The blue dashed lines denote the lunar terminator, and the black dashed lines denote the location where the SZA = 50° in (e)–(h).

between LP and the edge of the SPAB (the dark red area in Figures 1(f)–(h)) is about 30° or, correspondingly, ~ 900 km in distance along the lunar surface as shown in Figure 1(h).

The observations for Event II are displayed in Figures 1(i)–(p). In this event, the IMF remains unchanged from 6:55 UT to 7:45 UT on 1998 January 31. A strong enhancement in the field magnitude can be seen from 7:26 UT to 7:43 UT (Figure 1(k), between the two vertical dashed lines C and D) when LP passes by the downstream region of the SPAB LMA in the LSE coordinate system at an altitude of about 100 km (Figure 1(p)). The SPAB LMA is centered at SZA $\sim 40^\circ$ in the LSE coordinate system in this event, and the separation of LP with the SPAB LMA from C to D is also about 30° in longitude or 900 km in distance, the same as the previous event, except for a short period (from 7:27 UT to 7:30 UT) in which LP is very close to the strong lunar crustal magnetic fields.

The common feature of the aforementioned two events is that the field enhancements occur near the terminator in the LSE coordinate system where E_{SW} points to and downstream of the SPAB LMA. In both events, the SPAB LMA is located near the subsolar point, with the SZAs of 35° and 40° , respectively, far away from the lunar terminator. Due to the projection effect, the edge area of the SPAB LMA seems close to the lunar terminator. However, the separation angles between them are at least 30° or 900 km along the lunar surface. Thus, it is difficult to assert that the observed field enhancements are the compressed lunar crustal magnetic fields or the compressed IMF behind the possible limb shock (i.e., limb compression). The SPAB LMA locations being far away from the lunar terminator and the large separation between the SPAB LMA and LP suggest that some other mechanisms may act here.

3.2. Statistical Studies

The magnetic field enhancements commonly occurred during the journey of LP. Here, the statistical studies are conducted by using the 1.5 yr LP data in the LSE coordinate system. Figure 2 involves all the magnetic field observations when the Moon is in the solar wind ($SA_{S-E} > 90^\circ$). In Figures 2(a) and (b), the distributions of R_B near the terminator with SZA from 70° to 110° and at altitudes of 15–45 km (Figure 2(a)) and 85–115 km (Figure 2(b)), respectively, are unfolded by the SZA and displayed on the y_z -plane of the LSE coordinate system. The black dashed circles in Figures 2(a) and (b) denote the lunar terminator. Before the terminator, a clear asymmetry is shown in the low-altitude distribution of R_B in Figure 2(a). The averaged field enhancement reaches $R_B = 1.3$ before the left terminator, stronger than that at the same SZA on the right side ($R_B = 1.1$). At high altitudes, there is no clear pattern in the distributions to show the asymmetry in the enhancements (Figure 2(b)). Given that the observed magnetic field may be closely related to the crustal magnetic fields, we show the distribution of the modeled crustal magnetic fields, which are 10 km above the footprint of LP on the lunar surface (Figures 2(c) and (d)). It is seen that, at low altitudes, for the stronger field enhancement region ahead of the left terminator, the corresponding crustal magnetic fields are not stronger or are even weaker than those below the weaker field enhancement region on the opposite side (Figure 2(c)).

Behind the terminator, a left–right asymmetry also exists in the field reduction at low latitudes (Figure 2(a)). On the right, the reduction is significant and R_B is as low as 0.9. These field reductions are thought to be produced by the diamagnetic currents in the wake expansion region originating from the plasma pressure gradients in the direction perpendicular to the magnetic fields (Ness et al. 1968; Owen et al. 1996). However, the field reduction region disappears at low altitudes behind the

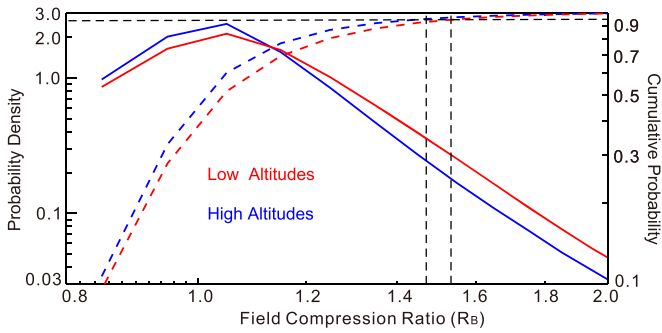


Figure 3. Probability densities (solid curves) and cumulative probabilities (dashed curves) of the field compression ratio at low altitudes (15–45 km, in red) and at high altitudes (85–115 km, in blue) around the lunar terminator (the solar wind zenith angle ranges from 70° to 110°). All the distributions are plotted in log–log format. The probabilities peak at $R_B \sim 1.0$ for both the low- and high-altitude cases because of many of the non-disturbed magnetic fields come into the statistics. At the long tails of the distributions ($R_B > 1.1$), the probabilities are systematically larger for the low-altitude case than those for the high-altitude case. The 95% percentiles for the cumulative probabilities indicate that the maximum field compression ratio R_B at the terminator may reach 1.5.

left terminator. At high altitudes, the field reductions behind the terminator (Figure 2(b)) exist, but no evident asymmetries are shown in Figure 2(b).

To further examine the whole structures of the field variations in the LSE coordinate system, the distributions of R_B at different altitudes are projected on the xy -plane as shown in Figures 2(e) and (f). The left–right asymmetries in the field variations are evident in the low-latitude projection in Figure 2(e). The fields are systematically enhanced ahead of the lunar terminator (the dark red region in Figure 2(e)) and stronger on the left than those on the right, the same as observed in Figure 2(a). Also, the most significant field reduction appears behind the right terminator and it is very weak behind the left terminator. On the contrary, at high altitudes (Figure 2(f)), the field reductions occur behind both the left and right terminator and they are more significant on the left. The locations of the field reduction regions are observed to be twisted toward the right behind the Moon, and the most significant field reduction region on the left is closer to the central wake than that on the right. Figures 2(g) and (f) show that neither the field enhancements nor the field reductions near the lunar terminator are related to any particular distribution of the lunar crustal magnetic fields, implying that these asymmetries are not produced directly by the crustal magnetic fields.

The statistics in Figure 2 involves all the observations in the database, including both the disturbed and the undisturbed field observations. Figure 3 gives the probability densities (the solid curves) and the cumulative probabilities (the dashed curves) of the field perturbations with SZA from 70° to 110° . It is seen that at both low and high altitudes, the peaks of probability densities are around $R_B = 1$, indicating that the undisturbed data dominate the statistics. The long tails are present in the distributions beyond $R_B = 1$, indicating that some of the magnetic fields at the terminator are indeed enhanced. The peaked probability density for the low-altitude case is smaller than that for the high-altitude case, but in the distribution tails (e.g., $R_B > 1.1$), the probability densities for the low-altitude case are systematically larger than those for the high-altitude case, indicating that the field enhancement is more significant at low altitudes. The 95% percentile is used to estimate the maximum compression ratio of the magnetic fields near the

lunar terminator (the horizontal dashed line on the top of Figure 3). It is found that the corresponding R_B can be ~ 1.5 for both altitudes around the terminator, which means that almost 95% of the data do not exceed 1.5. This value is consistent with the two aforementioned events.

4. Discussion

In this Letter, the lunar magnetic perturbations are investigated both in case studies and in statistics of the LP observations near the Moon. In the LSE coordinate system, the magnitudes of these enhancements exhibit a left–right asymmetric distribution, stronger before the left terminator than those before the right terminator. The left–right asymmetry can also be seen in the field reductions in the lunar wake expansion regions behind the terminator, and on the left, the field reductions are more significant and located closer to the central wake than those on the right.

Both the asymmetries in the field enhancement and reduction may arise from E_{sw} since the differences are present mainly between the two opposite left and right terminators, which E_{sw} points to and against, respectively (Cloutier et al. 1974; Dong et al. 2015). Although most of the incident solar wind particles are absorbed by the lunar surface, a fraction of them still can be reflected (Nishino et al. 2010; Wieser et al. 2010). Once reflected, these solar wind particles can be accelerated by E_{sw} to have large gyroradii (~ 400 km) comparable with the size of the Moon and to converge to the left terminator, resulting in an asymmetric plasma environment near the Moon (Holmström et al. 2010), which may eventually produce the observed asymmetric magnetic perturbations.

To quantitatively evaluate the influences of the solar wind reflection, a test particle model is established here. The quantities of the solar wind and the IMF parameters input into the model are the median values in the data set used. The solar wind bulk velocity is set to be 400 km s^{-1} in the $-x$ -direction. The solar wind plasma satisfies the shifted Maxwellian distribution, the number density is 6 cm^{-3} , and the temperature is 8.0 eV . In the data set, the median magnitude of the IMF is 6.5 nT and the cone angle is 94° . The model used can be three-dimensional, but in order to save the computing resource, only the two-dimensional version is applied on the equatorial plane and the motion of the simulated particles are confined within the xy -plane. In this case, for simplicity, the input IMF is fixed to the direction along the z -axis (cone angle = 90°). The E_{sw} points to the $-y$ -direction, and clearly, the coordinate system used here is indeed LSE according to its definition.

The detailed reflection properties, including the reflection velocity, reflection site, and reflection ratio, are all critical to the influence on the background plasma and magnetic environment. In this model, the speed of a reflected particle is set to be the same as its incident speed according to the satellite observations (Saito et al. 2010; Lue et al. 2011). However, the directional velocity distribution of the solar wind particles reflected over the lunar surface is not exactly known. There are different reflection functions of the velocity distribution explained by Holmström et al. (2010), such as specular reflection, perpendicular reflection, and \cos^2 -perpendicular reflection. Here, the \cos^2 -perpendicular reflection is adopted. In this situation, the reflection direction is set to be randomly distributed around the normal direction of the local lunar surface satisfying a distribution function as $\cos^2\theta$, where θ is the subtended angle between the reflection

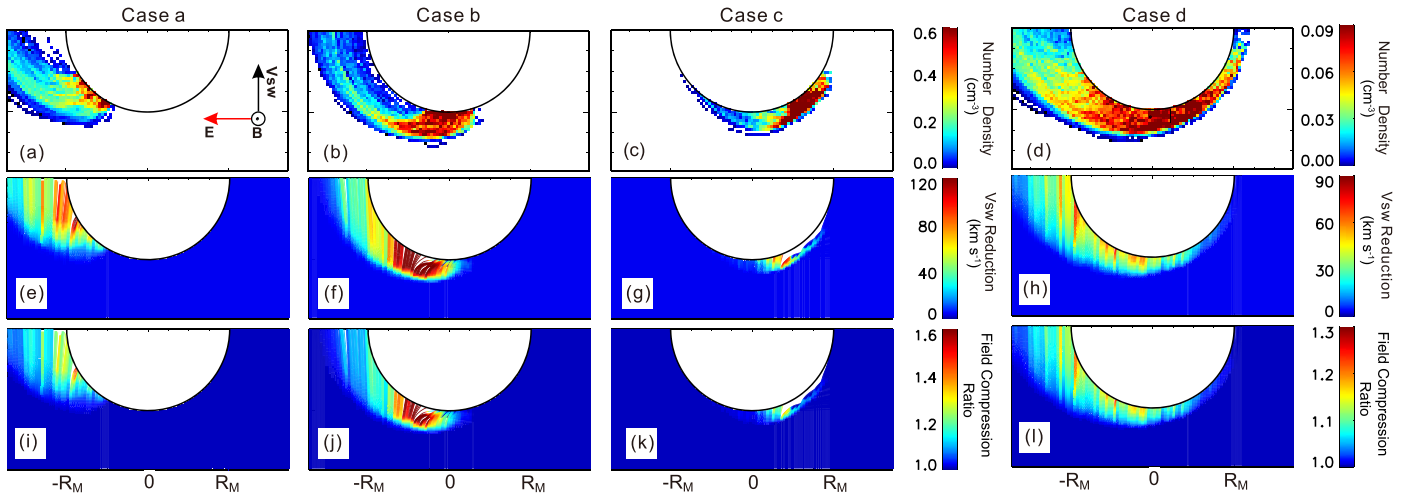


Figure 4. Results of four runs of the test particle model, Cases a–d, with the different locations of an LMA and the different reflection ratios. In Cases a–c, the LMA is centered at $(0.87, -0.5)R_M$, $(1.0, 0)R_M$, and $(0.87, 0.5)R_M$, respectively, and the reflection ratios are all set to be 10%. In Case d, the incident solar wind can be reflected all across the dayside surface of the Moon at a reflection ratio of 1%, representing an average situation or the unmagnetized lunar soil reflection situation. From top to bottom, each panel shows the number density of the reflection particles ((a)–(d)), the deceleration of the solar wind ((e)–(h)), and the field compression ratio ((i)–(l)).

direction and the normal direction of the local surface at the reflection site. In fact, it does not matter what type of reflection is chosen here, and as already verified by Fatemi et al. (2014) that the global plasma environment around the Moon is not sensitive to the reflection function, particularly the reflection direction. Solar wind particles can be reflected almost everywhere on the dayside of the Moon; the reflection ratio, however, is remarkable only above the LMAs (e.g., Saito et al. 2010; Lue et al. 2011). We focus on the large LMA group, i.e., the SPAB LMA, located at the farside with center at $(170^\circ\text{E}, 30^\circ\text{S})$. In the LSE coordinate system, the latitude and the longitude of SPAB LMA can be of any quantities depending on the V_{SW} , the IMF direction, and the lunar phase. In this study, the test particle method is applied to three cases, a–c, with different LMA locations to simulate the influence of the reflection site. In Cases a–c, the LMA is centered at $(0.87, -0.5)R_M$, $(1.0, 0)R_M$, and $(0.87, 0.5)R_M$, respectively, in the xy -plane of the LSE coordinate system. The diameter of the SPAB LMA is set to be 1000 km, i.e., the incident solar wind can be reflected over a 1000 km area on the lunar surface while all the particles impacting elsewhere are absorbed. The reflection ratio is set to be 10%. An additional case (Case d) is run to represent the averaged situation, and the incident solar wind particles are allowed to reflect on the whole dayside surface but the reflection ratio is reduced to be as low as 1%. Clearly, Case d may also represent the situation that the incident solar wind particles are reflected by the lunar regolith on the whole unmagnetized lunar surface since the reflected ratio of the regolith is suggested to be of the same quantity of 1% (Saito et al. 2008; Wieser et al. 2010).

The calculated results for all four cases are shown in Figure 4, including the number density of the reflected particles (Figures 4(a)–(d)), the deceleration of the background solar wind (Figures 4(e)–(h)), and the field compression ratio (Figures 4(i)–(l)), respectively. After reflection, these particles are picked up by the background solar wind, and in turn, to maintain the momentum conservation, these accelerated particles will slow down the background solar wind. The deceleration of the background solar wind (Figures 4(e)–(h)) is calculated through the momentum conservation law, i.e., the

momentum loss of the background solar wind is equal to the momentum gain of the reflected particles. In a steady state, the magnetic flux conservation allows us to calculate the enhancement in the magnetic field, and further to calculate the compression ratio of the enhanced magnetic field around the Moon to the background IMF (Figures 4(i)–(l)). It is clear in Figures 4(a) and (b) when the LMA is located on the left side or subsolar point, all the reflected particles move along with \mathbf{E}_{SW} and converge toward the left terminator, making an asymmetric plasma environment in front of the Moon. The reflection ratio of 10% gives the field compression ratio of ~ 1.2 at the left terminator (Figures 4(i) and (j)). In Case d, which represents the averaged or the statistical situation, the left–right asymmetries are clearly seen in all the parameters. At the right terminator in Figure 4(d), the reflected particles seem denser and they just reach the 200 km altitude before returning to the lunar surface and absorbed (the secondary reflection is not allowed in this model). At the left terminator, however, the reflected particles can arrive at much higher altitudes and occupy a wider area. Under this condition, the solar wind that passes through this area will be significantly decelerated, leading to a stronger compression for the IMF ($R_B \sim 1.2$), which is comparable with the statistical results shown in Figure 2(e). The model used in this study is simplified, and the electric and magnetic fields are not self-consistent, which may lead to some problems. For example, in Case c, the solar wind particles cannot even arrive at the lunar surface because of too dramatic deceleration. A self-consistent PIC model is desired for further study.

Figure 5 shows the probability density of the SPAB LMA center as a function of the Y (red line) and Z (blue line) coordinates in the LSE coordinate system. The SPAB LMA is seen to be evenly located along the z -axis, and the probability density peaks at $-0.5R_M$ and $0.5R_M$ along the y -axis respectively. The probability at $Y = 0.5R_M$ is the highest; in this case, however, the reflected particles will impact on the lunar surface immediately after the reflection as shown in Figure 4(c), and they can neither reach a high altitude nor affect the plasma or magnetic field environment significantly. In contrast, when the SPAB LMA center is located at

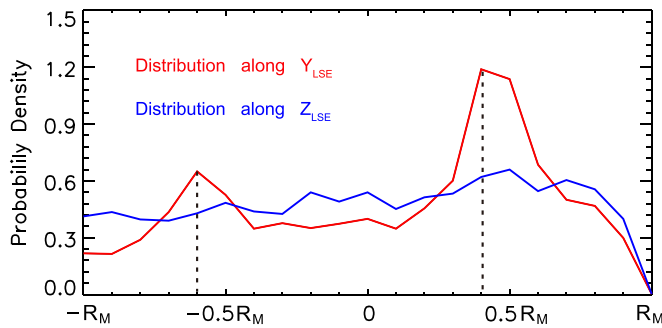


Figure 5. Probability density of the location of the SPAB LMA center (170°E , 30°S in the SEL coordinate system) as a function of the Y (red line) and Z (blue line) coordinates, respectively, in the LSE coordinate system. The probability density peaks at $Y = -0.5R_M$ and $Y = 0.5R_M$, respectively, and the probability density at $Y = 0.5R_M$ is higher than that at $Y = -0.5R_M$.

$Y = -0.5R_M$, the effect of the reflected particle on the terminator region will be as remarkable as shown in Figures 4(a), (e), and (i). Case a with the LMA centered at $(0.87, -0.5)R_M$ thus represents the distribution peak at $Y = -0.5R_M$ in Figure 5, and this situation may dominate the statistical field enhancement at the left terminator as observed in Figures 2(e) and (f). When the SPAB LMA center is located near the subsolar point, the reflected particles will affect the dayside region as well as the terminator area (Figures 4(b), (f), and (j)). Since the probability density of the condition that the SPAB LMA is centered near the subsolar point is low, the field enhancement over the left dayside surface is thus as insignificant as that at the left terminator (Figures 2(e) and (f)).

Although our model cannot be used to describe the lunar wake properties, the left–right asymmetric plasma environment on the dayside of the Moon can be attributed to the asymmetric field reductions in the wake expansion regions right behind the lunar terminator. At the left terminator, the plasma should be denser than that at the opposite terminator because of the additional reflected solar wind. The stronger pressure gradients thus exist on the left wake boundary, producing a stronger and wider diamagnetic current, and leading to a more significant and wider field reduction there. Although the magnetic reduction is more significant and wider behind the left terminator, the net reduction of the magnetic field could be smaller than that on the right side, particularly at low altitudes as seen in Figures 2(a) and (e). This is because the upstream background magnetic fields in front of the left terminator are also stronger and they have been compressed significantly by the reflected solar wind. At higher altitudes behind the left terminator, particularly in the region closer to the central wake, significant field reduction is dominant, i.e., the net field reduction is more dramatic, and is located closer to the central wake as seen in Figure 2(f).

5. Summary

Magnetic perturbations near the Moon characterize the solar wind interaction of the Moon or the LMAs. In the LSE coordinate system determined by V_{SW} and E_{SW} , the magnetic enhancements in front of the lunar terminator exhibit a clear left–right asymmetry, i.e., the $\pm Y$ asymmetry. The nominal Parker spiral magnetic field at the Moon is essentially in the ecliptic plane, and in this situation, the $\pm Y$ asymmetry is in fact on average in the north–south direction, i.e., along the normal direction to the ecliptic. The results of the test particle model

show that, besides the limb compression, the pickup process of the reflected solar wind particles may be a new mechanism to enhance the magnetic field around the Moon, particularly at the lunar terminator where E_{SW} points to. The field reductions in the expansion region of the lunar wake also exhibit an asymmetry between the two opposite terminator regions along the direction of E_{SW} , which is possibly produced by the asymmetric plasma environment arising from the reflected solar wind particles. The asymmetric plasma and magnetic fields associated with the pickup of reflected particles may be the common and nonnegligible element during the solar wind interaction of a small-scale magnetic field, such as that of an asteroid or a comet.

This work was supported by the B-type Strategic Priority Program of the Chinese Academy of Sciences (XDB41000000) and the National Natural Science Foundation of China (41731068, 41774175, and 41941001). We thank the Planetary Plasma Interactions (PPI) Node of the Planetary Plasma Interactions (PDS) at the Department of Earth Planetary, and Space Sciences at the University of California, Los Angeles (UCLA): <https://pds-ppi.igpp.ucla.edu> for providing the magnetic field observations from the Lunar Prospector mission and the NASA/GSFC’s Space Physics Data Facility for the OMNIWeb service at <http://cdaweb.gsfc.nasa.gov/> for providing the data for the solar wind and the interplanetary magnetic fields. We thank Dr. K.K. Kuranna at UCLA and Dr. Hengci Tian at IGGCAS for valuable discussions and suggestions. We also thank one anonymous reviewer for the thorough reviews and constructive comments.

ORCID iDs

Tian-Xin Zhang <https://orcid.org/0000-0001-5535-2976>
 Hui Zhang <https://orcid.org/0000-0002-3680-4989>
 Hai-Rong Lai <https://orcid.org/0000-0001-5750-7919>
 Jun Zhong <https://orcid.org/0000-0003-4187-3361>
 Jun Cui <https://orcid.org/0000-0002-4721-8184>

References

- Binder, A. B. 1998, *Sci*, **281**, 1475
 Blewett, D. T., Coman, E. I., Hawke, B. R., et al. 2011, *JGRE*, **116**, E02002
 Burinskaya, T. M. 2015, *P&SS*, **115**, 64
 Cloutier, P. A., Daniell, R. E., & Butler, D. M. 1974, *P&SS*, **22**, 967
 Colburn, D. S., Currie, R. G., Mihalov, J. D., & Sonett, C. P. 1967, *Sci*, **158**, 1040
 Dong, Y., Fang, X., Brain, D. A., et al. 2015, *GeoRL*, **42**, 8942
 Fatemi, S., Holmström, M., Futaana, Y., et al. 2014, *JGRA*, **119**, 6095
 Fatemi, S., Holmström, M., Futaana, Y., Barabash, S., & Lue, C. 2013, *GeoRL*, **40**, 17
 Futaana, Y., Machida, S., Saito, Y., Matsuoka, A., & Hayakawa, H. 2003, *JGRA*, **108**, 1025
 Giacalone, J., & Hood, L. L. 2015, *JGRA*, **120**, 4081
 Halekas, J. S., Brain, D. A., Mitchell, D. L., Lin, R. P., & Harrison, L. 2006, *GeoRL*, **33**, L08106
 Halekas, J. S., Delory, G. T., Lin, R. P., Stubbs, T. J., & Farrell, W. M. 2008, *JGRA*, **113**, A09102
 Halekas, J. S., Poppe, A. R., Lue, C., Farrell, W. M., & McFadden, J. P. 2017, *JGRA*, **122**, 6240
 Halekas, J. S., Poppe, A. R., McFadden, J. P., et al. 2014, *GeoRL*, **41**, 7436
 Halekas, J. S., Saito, Y., Delory, G. T., & Farrell, W. M. 2011, *P&SS*, **59**, 1681
 Harnett, E. M., & Winglee, R. M. 2000, *JGR*, **105**, 24997
 Harnett, E. M., & Winglee, R. M. 2003, *JGRA*, **108**, 1088
 Holmström, M., Wieser, M., Barabash, S., Futaana, Y., & Bhardwaj, A. 2010, *JGRA*, **115**, A06206
 Hood, L. L. 2011, *Icar*, **211**, 1109
 Hood, L. L., Richmond, N. C., & Spudis, P. D. 2013, *JGRE*, **118**, 1265

- Hood, L. L., & Schubert, G. 1980, *Sci*, **208**, 49
- Lin, R. P., Mitchell, D. L., Curtis, D. W., et al. 1998, *Sci*, **281**, 1480
- Lue, C., Futaana, Y., Barabash, S., et al. 2011, *GeoRL*, **38**, L03202
- Lue, C., Futaana, Y., Barabash, S., et al. 2014, *JGRE*, **119**, 968
- Mitchell, D. L., Halekas, J. S., Lin, R. P., et al. 2008, *Icar*, **194**, 401
- Ness, N. F., Behannon, K. W., Scarce, C. S., & Cantarano, S. C. 1967, *JGR*, **72**, 5769
- Ness, N. F., Behannon, K. W., Taylor, H. E., & Whang, Y. C. 1968, *JGR*, **73**, 3421
- Nishino, M. N., Fujimoto, M., Saito, Y., et al. 2010, *GeoRL*, **37**, L12106
- Owen, C. J., Lepping, R. P., Ogilvie, K. W., et al. 1996, *GeoRL*, **23**, 1263
- Purucker, M. 2008, *Icar*, **197**, 19
- Richmond, N. C., & Hood, L. L. 2008, *JGRE*, **113**, E02010
- Russell, C. T., & Lichtenstein, B. R. 1975, *JGR*, **80**, 4700
- Saito, Y., Yokota, S., Asamura, K., et al. 2010, *SSRv*, **154**, 265
- Saito, Y., Yokota, S., Tanaka, T., et al. 2008, *GeoRL*, **35**, L24205
- Sonett, C. P. 1982, *RvGSP*, **20**, 411
- Sonett, C. P., & Mihalov, J. D. 1972, *JGR*, **77**, 588
- Walker, R. J., & Russell, C. T. 2013, Magnetic Field Data from the Lunar Prospector Magnetometer, NASA Planetary Data System, LP-L-MAG-4-SUMM-LUNARCRDS-5SEC-V1.0, <https://pds-ppi.igpp.ucla.edu/search/view/?f=yes&id=pds://PPI/LP-L-MAG-4-SUMM-LUNARCRDS-5SEC-V1.0>
- Whang, Y. C., & Ness, N. F. 1970, *JGR*, **75**, 6002
- Wieser, M., Barabash, S., Futaana, Y., et al. 2010, *GeoRL*, **37**, L05103
- Zhang, H., Khurana, K. K., Kivelson, M. G., et al. 2014, *JGRA*, **119**, 5220
- Zhang, H., Khurana, K. K., Zong, Q. G., et al. 2012, *GeoRL*, **39**, L18104
- Zhong, J., Xie, L., Zhang, H., et al. 2013, *P&SS*, **79**, 56